Ultra-High-Crystallinity Transparent Glass-Ceramic Scintillators for High-Temperature X-Ray Imaging

Journal:	*SCIENCE CHINA Materials*
Manuscript ID	SCMs-2026-1080.R1
Manuscript Type:	Article
Date Submitted by the Author:	21-May-2026
Complete List of Authors:	Lin, Shisheng; Fujian Normal University Zhang, Yunfei; Fujian Normal University Gu, Rujian; Fujian Normal University Lin, Jidong; Fujian Normal University Qiao, Xvsheng Zeng, Lingwei Lin, Hewen; Fujian Normal University Zheng, Jiamin; Fujian Normal University Yang, Xiuxia; Kunming University of Science and Technology Xu, Xuhui Huang, Feng; Fujian Normal University Chen, Daqin; Fujian Normal University,
Keywords:	glass-ceramics, thermal stability, X-ray excited luminescence, X-ray imaging, optical materials
Speciality:	Optoelectronic Materials

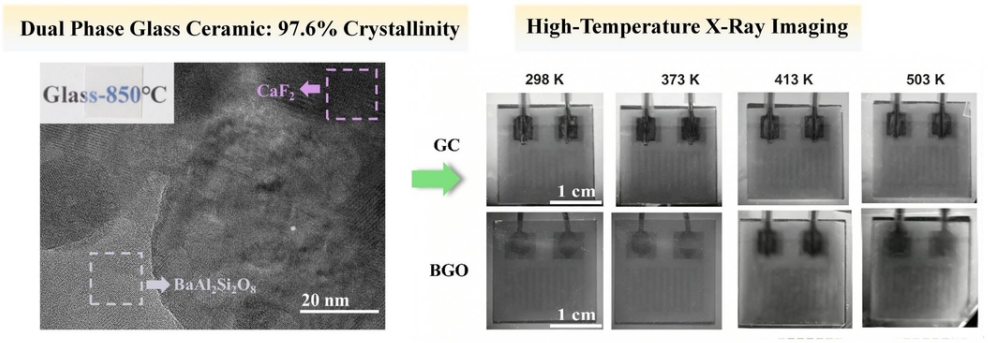

90x31mm (300 x 300 DPI)

Ultra-High-Crystallinity Transparent Glass-Ceramic Scintillators for High-Temperature X-Ray Imaging

Shisheng Lin [1, +], Yunfei Zhang [1, +], Rujian Gu [1], Jidong Lin [1, *], Xusheng Qiao [2], Lingwei Zeng [3], Hewen Lin [1], Jiamin Zheng [1], Xiuxia Yang [4, *], Xuhui Xu [4], Feng Huang [1], Daqin Chen [1, 5, *]

[1] Dr. S. S. Lin, Y. F. Zhang, R. J. Gu, J. D. Lin, H. W. Lin, J. M. Zheng, Prof. F. Huang, Prof. D. Q. Chen

College of Physics and Energy, Fujian Normal University, Fuzhou, 350117, P. R. China

E-mail: jdlin@fjnu.edu.cn (J. D. Lin); dqchen@fjnu.edu.cn (D. Q. Chen)

[2] Dr. X. S. Qiao

State Key Laboratory of Silicon Materials & School of Materials Science and Engineering, Zhejiang University, Hangzhou, 310027, P. R. China

[3] Dr. L. W. Zeng

School of Chemistry and Chemical Engineering, Hunan University of Science and Technology, Xiangtan, 411201, P. R. China

[4] Dr. X. X. Yang, Prof. X. H. Xu

Faculty of Materials Science and Engineering, Key Laboratory of Advanced Materials of Yunnan Province, Kunming University of Science and Technology, Kunming, 650093, P. R. China

E-mail: xiuxia941129@163.com (X. X. Yang);

[5] Prof. D. Q. Chen

Fujian Provincial Engineering Technology Research Center of Solar Energy Conversion and Energy Storage, Fuzhou, 350117, P. R. China

[+] These authors contributed equally to this work

ABSTRACT

High-temperature X-ray imaging requires scintillators of high crystallinity, efficient scintillation, and robust thermal stability, yet suitable scintillators remain scarce. In this study, an ultra-high-crystallinity transparent glass-ceramic (GC) scintillator is strategically designed through a controllable heat-treatment-induced crystallization process. A sequential precipitation method is employed, where cubic CaF_2 nanocrystals initially form, subsequently promoting the heterogeneous nucleation and growth of hexagonal $BaAl_2Si_2O_8$. Due to intrinsic nanoscale phase separation into F-rich and O-rich domains, atomic diffusion distances are significantly reduced, resulting in an unprecedented crystallinity of up to 97.6 %. Notably, the presence of defect traps (oxygen vacancy defects, likely located within the lattice or at the crystalline/amorphous interface) enables efficient carrier capture and thermally stimulated release, contributing to remarkable resistance to thermal quenching. Consequently, the proposed GC scintillator maintains 90.6 % of its integrated X-ray excited luminescence (XEL) intensity at 300 °C, with the integrated XEL intensity reaching 94.2 % of the commercial $Bi_4Ge_3O_{12}$ (BGO) at room temperature, thus enabling stable high-temperature X-ray imaging with a spatial resolution of ~10.4 lp/mm up to 225 °C. This work provides a versatile pathway for developing high-sensitivity scintillators for extreme-environment X-ray imaging.

Keywords: glass-ceramics; thermal stability; X-ray excited luminescence; X-ray imaging; optical materials.

1. Introduction

X-ray imaging technology has been widely used in security inspection, industrial nondestructive inspection, medical diagnosis, and scientific research[1,2,3,4,5,6]. The increasing demand for higher-quality X-ray imaging has driven the development of techniques capable of industrial detecting the internal structures of equipment under diverse conditions, such as high temperatures, which is crucial for ensuring machine safety and reliability in extreme conditions[7]. Evidently, the need for advanced high-temperature X-ray imaging technology necessitates significant advancements in high-thermal-stability scintillators.

In this context, all-inorganic scintillators, including single crystals, phosphor ceramics, amorphous glasses, and glass ceramics (GC), are more suitable than organic materials, due to their superior physical/chemical stability[8,9]. In fact, although single-crystal scintillators, such as $Bi_4Ge_3O_{12}$ (BGO) and CsI: Tl, have been predominant commercially accessible, they are still generally characterized by poor thermal quenching resistance[10]. Moreover, their widespread use is constrained by complex manufacturing processes, limited luminescence wavelengths, and challenges in shaping[11]. Meanwhile, ceramic scintillators also encounter inherent challenges, such as long production cycles and a restricted selection of high-thermal-stability hosts[12], while glass scintillators suffer from low light yields due to unavoidable defects in amorphous structure[13,14]. In contrast, GC scintillators have the advantages of cost-effective fabrication, flexible high-thermal-stability low-phonon-energy host design, tunable luminescence, being easily drawn into fibers or large-size production, thus having received great attention[15,16,17,18].

Specifically, the development of GC scintillators is relatively recent, dating back to the early 21st century[19]. Thereafter, significant endeavors have been dedicated to fabricate high-quality

GC scintillators, encompassing systems such as tellurite, oxyfluoride, and halide, among others[20,21,22,23,24,25,26]. For example, the advancement of an Eu-doped $CsPbBr_3$ perovskite GC scintillator has led to high-resolution X-ray imaging (15.0 lp/mm) with markedly diminished light scattering and enhanced stability[27]. Meanwhile, an ionic-covalent hybrid network strategy helps develop $BaCl_2$: Eu^{2+} nanocrystal-based GC, resulting in a relatively high precipitation fraction (~37 %) of nanocrystals within the GC, and further significantly enhancing scintillation efficiency and imaging resolution[28]. Numerous studies underscore the promising future of GC scintillators, facilitating substantial advancements in X-ray imaging applications. However, GC scintillators still encounter a critical challenge: the "performance dilution effect" caused by the limited content of luminescent counterparts in GC. The issue of inadequate scintillation properties resulting from low crystallinity and the consequent reduced light yield severely hampers the performance of X-ray imaging. Consequently, there is an urgent demand for the development of ultra-high-crystallinity (>90%) transparent GC scintillators, particularly those of superior thermal stability to meet the critical requirements of high-temperature X-ray imaging applications.

In this study, an ultra-high-crystallinity transparent GC scintillator is strategically designed through a controllable heat-treatment-induced crystallization process. A sequential precipitation method is employed, with which cubic CaF_2 nanocrystals initially form and subsequently promote the heterogeneous nucleation and growth of hexagonal $BaAl_2Si_2O_8$. This crystallization process is facilitated by intrinsic nanoscale phase separation into F-rich and O-rich domains, effectively reducing atomic diffusion distances and enabling an exceptional ultra-high crystallinity of 97.6 %. Simultaneously, the nanoscale CaF_2 crystallites and the predominant $BaAl_2Si_2O_8$ matrix mitigate light scattering, preserving the GC' visible-light transmittance of 69.4 %. This crystallinity is

higher than that of most reported transparent GC systems while optical transparency is retained (Table S1). More importantly, defect traps (oxygen vacancy defects) efficiently capture radiation-induced carriers and facilitate their thermally stimulated release at elevated temperatures, leading to exceptional resistance to thermal quenching. Consequently, the proposed GC maintains 90.6 % of its integrated X-ray excited luminescence (XEL) intensity at 300 °C, significantly surpassing that of commercial BGO scintillators. Combined with a competitive scintillation performance and stable imaging performance, this work presents a viable solution and a universal design framework for high-sensitivity X-ray imaging under extreme thermal conditions.

2. Results and discussion

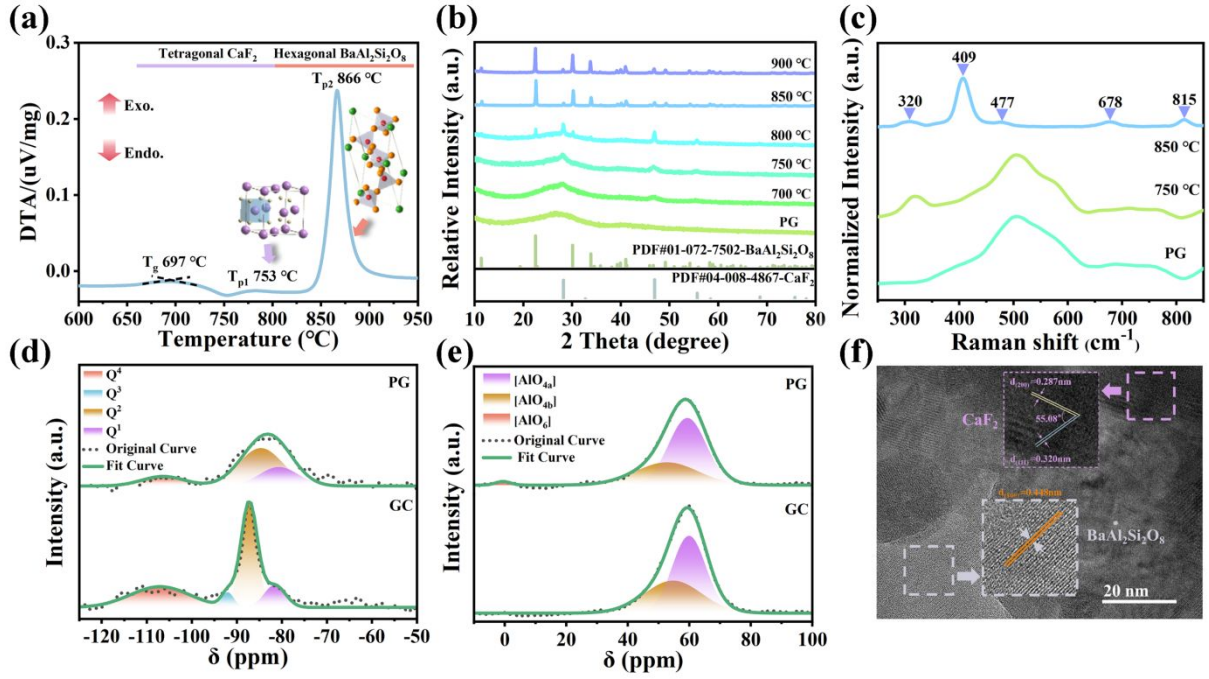

Figure 1. (a) DSC curve of PG, showing the T_g, T_{p1} and T_{p2}; the insets depict the crystal structures corresponding to the exothermic crystallization peaks, namely tetragonal CaF_2 and hexagonal $BaAl_2Si_2O_8$. (b) XRD patterns of PG and GC heat-treated at various temperatures (700-900 °C). (c) Raman spectra of PG and GC heat-treated at 750 and 850 °C. (d) ^{29}Si MAS NMR spectra and (e) ^{27}Al MAS NMR spectra of PG and GC. (f) HRTEM image of GC; the insets present locally magnified regions.

The differential scanning calorimetry (DSC) analysis reveals that the glass transition temperature (T_g) of the precursor glass (PG) is 697 °C, with two exothermic crystallization peaks (T_p) detected at 753 °C and 866 °C (Figure 1a). Accordingly, the PG was subsequently subjected to heat treatment at temperatures between 700 °C and 900 °C. Upon heat treatment, the X-ray diffraction (XRD) pattern initially retained amorphous characteristics while showing the diffraction peaks of cubic CaF_2 at heat-treatment temperature of 700 °C; as heat-treatment temperature increased, distinct hexagonal $BaAl_2Si_2O_8$ diffraction peaks appeared at 800 °C, and their relative intensity grew significantly at 850 °C, leading to a corresponding total crystallinity as high as 97.6 % (Figure 1b and Table S2). The corresponding crystallinity calculation is provided in the Supporting Information (Supplementary Note 1). Evidently, combining the DSC and XRD results, the two exothermic crystallization peaks at 753 °C and 866 °C can be attributed to the formation of cubic CaF_2 and hexagonal $BaAl_2Si_2O_8$, respectively, which suggests that upon thermal activation, the metastable PG initially precipitates CaF_2, followed by $BaAl_2Si_2O_8$. As shown in the Raman spectra of Figure 1c, the peak at 320 cm^{-1} can be attributed to the Ca-F vibration resulting from the precipitation of the CaF_2, which becomes distinctly visible upon CaF_2 formation. The characteristic peak at 409 cm^{-1}, corresponding to the Ba-O stretching vibration, and the broad absorption band at 815 cm^{-1}, associated with the Si-O stretching vibration, are both significantly enhanced following the precipitation of the $BaAl_2Si_2O_8$, as these coordination bonds are present within its crystal structure. The broad peak around 678 cm^{-1} originates from the symmetric stretching vibration of [AlO_4], and the remaining peaks are difficult to assign. These results further confirm the sequential high crystallinity precipitation of the CaF_2 and $BaAl_2Si_2O_8$ in the composite. Further, Figure 1d presents the ^{29}Si magic-angle spinning nuclear magnetic

resonance (MAS-NMR) spectra of PG and GC (heat-treated at 850 °C), where a significant change in the signal shape was observed as the material form transitions from PG to GC. This indicates an obvious structural transformation, specifically, the Q^1 species with a single bridging oxygen evolves into Q^2-Q^4 species with an increased number of bridging oxygens, providing evidence for the formation of a rigid structure composed of interconnected [SiO_4] tetrahedra (Table S3). Additionally, the peaks become sharper, approaching the nuclear magnetic resonance (NMR) characteristics typical of crystalline phases. Meanwhile, the ^{27}Al MAS-NMR spectra reveal that the distorted [AlO_{4b}] species within PG disappears upon the formation of GC, because of the transition from a disordered long-range amorphous structure to a highly ordered long-range total framework derived from the high crystallinity (Figure 1e and Table S3). The transmission electron microscopy (TEM) image of the GC reveals numerous lattice fringes and demonstrates high crystallinity of the composite (Figure 1f). The crystalline phases can be further identified by measuring the interplanar distances and the angles between various lattice planes: (1) The lattice fringes, with interplanar spacings of 0.448 nm, correspond to the (100) plane of hexagonal $BaAl_2Si_2O_8$; (2) The lattice fringes with interplanar spacings of 0.287 nm and 0.320 nm are assigned to the (200) and (111) planes of cubic CaF_2, with the measured angle of 55.08° aligning closely with the theoretical value (54.74°).

Moreover, energy dispersive spectroscopy (EDS) elemental mapping clearly reveals that within the matrix predominantly composed of Ba, Al and Si, which corresponds to the $BaAl_2Si_2O_8$ crystalline phase, the elements Ca and F exhibit localized nanoscale enrichment with approximately rounded features (~60 nm), indicating the formation of CaF_2 nanocrystals (Figure 2a). These results unequivocally confirm that the CaF_2 nanocrystals are indeed embedded within

the $BaAl_2Si_2O_8$ phase. It can be inferred that CaF_2 precipitates first from the glass, followed by heterogeneous nucleation and growth of $BaAl_2Si_2O_8$ on the surfaces of the preformed CaF_2 crystallites. Meanwhile, the Tb element displays a uniform spatial distribution throughout the GC, suggesting that Tb^{3+} are homogeneously incorporated into the lattice structures of both the CaF_2 and $BaAl_2Si_2O_8$ crystalline phases. The molecular dynamics (MD) simulation reveals that the component distribution within the PG is inherently inhomogeneous at the nanoscale, exhibiting distinct phase separation into F-enriched and O-enriched domains (Figure 2b and Supplementary Note 2), thus providing the essential structural preconditions for the sequential nucleation and growth of fluoride and oxide crystalline phases within their respective regions. Additionally, regarding the site occupancy of Tb^{3+}, they can evidently substitute for Ca^{2+} in the CaF_2 (Figure S1), whereas in the $BaAl_2Si_2O_8$ phase, the substitution of Tb^{3+} for Al^{3+} with a smallest formation energy of 0.93 eV suggests that Tb^{3+} ions are most likely to occupy Al^{3+} lattice sites (Figure 2c and Supplementary Note 3).

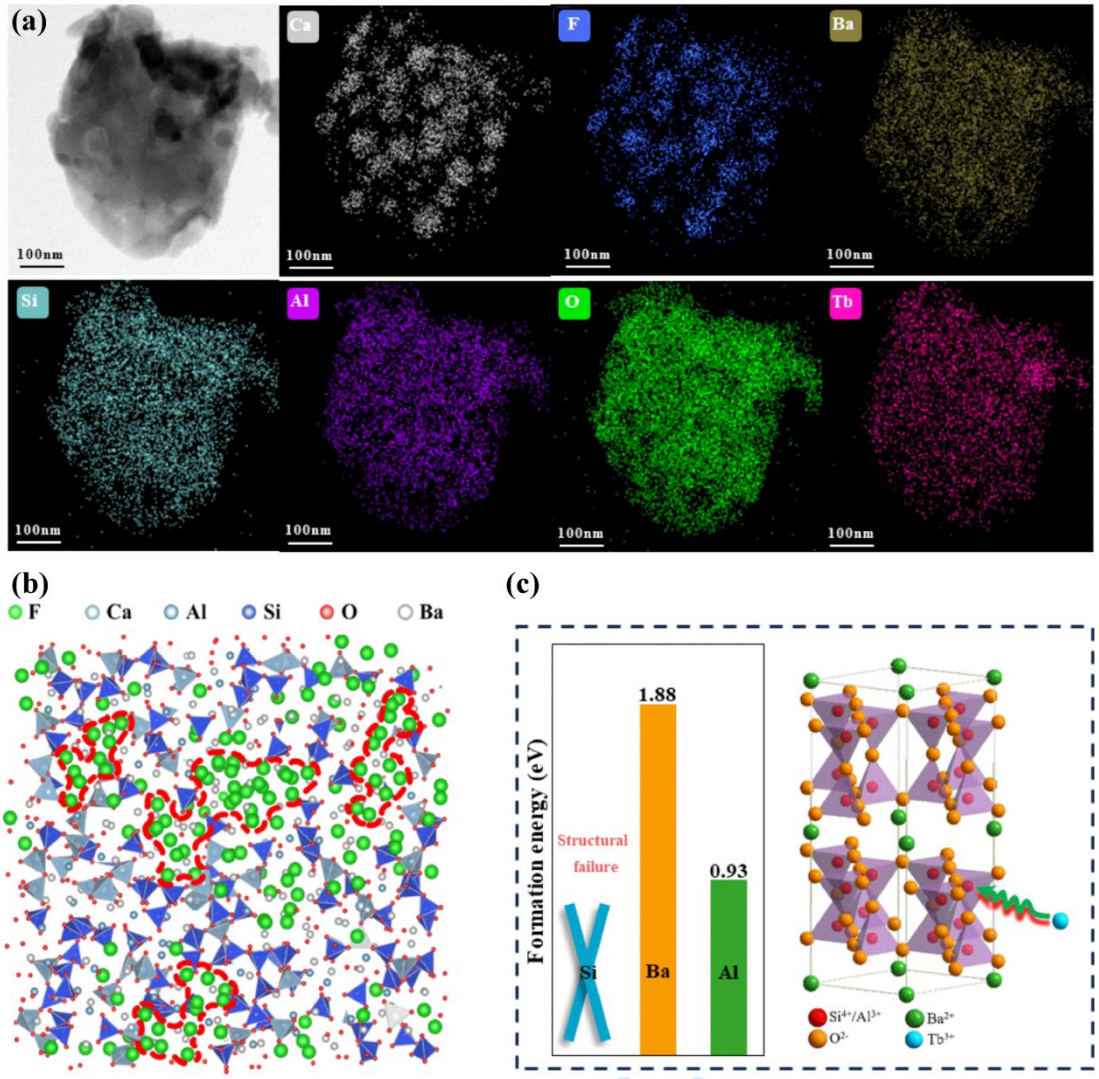

Figure 2. (a) TEM image and corresponding EDS elemental mappings of proposed ultra-high-crystallinity GC, showing the spatial distributions of Ca, F, Ba, Si, Al, O and Tb. (b) Representative atomic structures obtained from MD simulations of PG. (c) Calculated formation energies of Tb^{3+} substitution at different crystallographic lattice sites (Si, Ba, and Al) in hexagonal $BaAl_2Si_2O_8$; the inset illustrates the corresponding substitutional configurations.

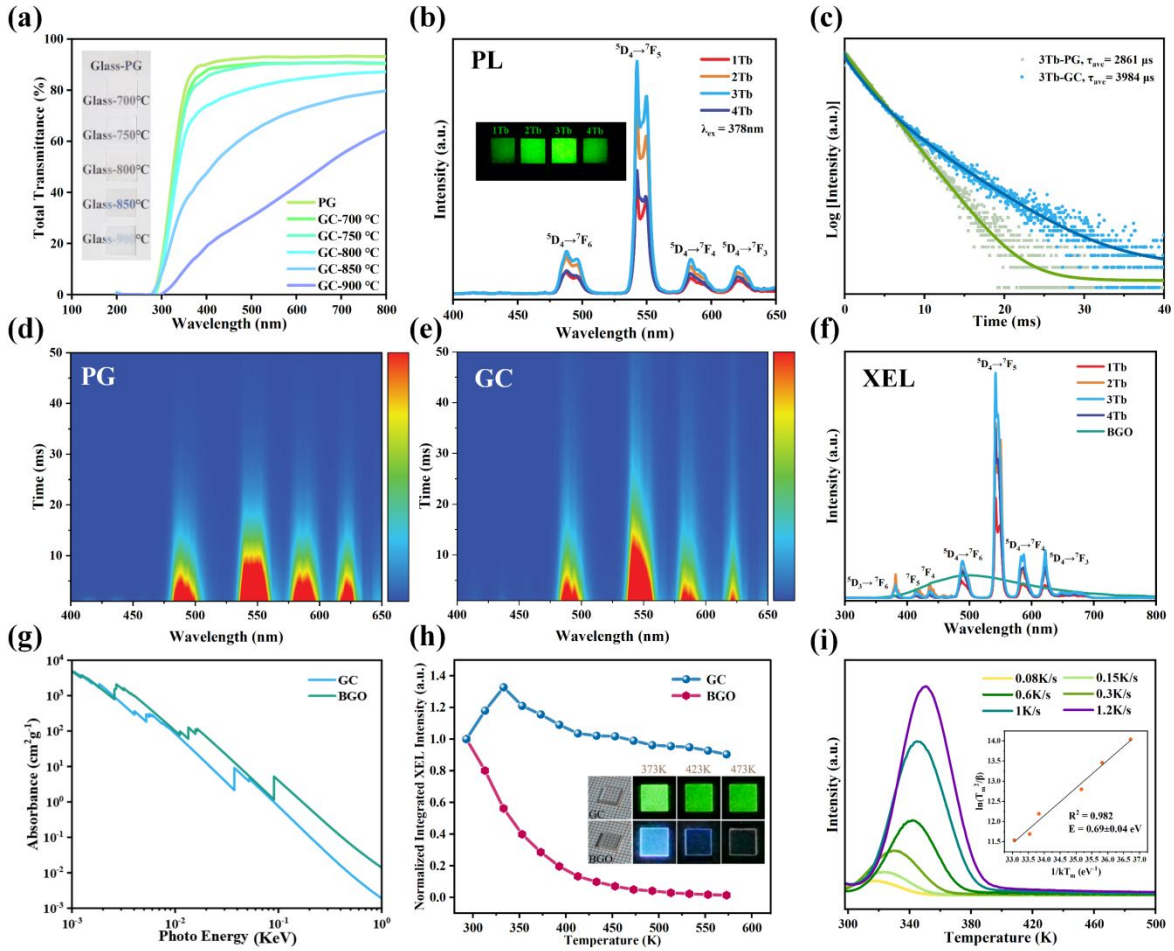

Figure 3. (a) UV-vis transmittance spectra of the PG and GC heat-treated at different temperatures. (b) PL spectra of Tb^{3+}-doped GC with varying Tb^{3+} concentrations under 378 nm excitation; the inset displays the corresponding luminescence photographs. (c) PL decay curves of 3Tb-PG and 3Tb-GC. TRPL of (d) PG and (e) GC. (f) XEL spectra of GC with different Tb^{3+} concentrations. (g) X-ray absorption coefficients of GC and commercial BGO as a function of photon energy. (h) Temperature-dependent normalized integrated XEL intensity of GC and BGO; the inset shows the corresponding XEL photographs recorded at various temperatures. (i) TL spectra of GC measured at different heating rates; the inset illustrates the linear fitting results.

In terms of optical transparency, the optimized ultra-high crystalline GC (heat-treated at 850 °C) maintained a transmittance of ~ 69.4 %. Specifically, the transparency of composite materials is primarily influenced by light scattering at the interfaces between distinct phases. The ultra-

high-crystallinity GC maintain transparency, possibly due to the nanoscale size of CaF_2 and the high content of $BaAl_2Si_2O_8$ matrix, and the extremely low concentration of the residual amorphous phase (Figure 3a). However, as the heat treatment temperature increases from 750 to 900 °C, the visible light transmittance of the GC gradually decreases from 89.8 % to 42.4 %, attributed to the continuous growth of $BaAl_2Si_2O_8$ (Figure 1b, Figure 3a and Figure S2). As shown in Figure 3b, Tb^{3+} concentration d UV ependent photoluminescence (PL) spectra of GC under 378 nm excitation reveal that the luminescence intensity of Tb^{3+} gradually enhances until 3 mol%, before significant concentration quenching occurs due to cross-relaxation between Tb^{3+} ions (Figures S3 and S4). It was also observed in the XEL behavior (Figure 3f). The transient luminescent decay curves of PG and ultra-high-crystallinity GC exhibit lifetimes in the millisecond range (Figure 3c). Notably, when the material form transitions from PG to GC, the lifetime increases significantly from 2.861 ms to 3.984 ms due to the decreasing possibility of non-radiative relaxation. Meanwhile, the fitting method changes from a single exponential fit (attributable to Tb^{3+} in the amorphous structure) to a multi-exponential fit (corresponding to Tb^{3+} in CaF_2, $BaAl_2Si_2O_8$ and residual amorphous phase). Further, time-resolved photoluminescence spectroscopies (TRPL) validate the observed trend in luminescence lifetime (Figures 3d and 3e). At different delay times, the emission profile consistently corresponds to the characteristic Tb^{3+} emission, with no shift in the peak position, confirming that the luminescent center is only Tb^{3+} (Figures 3d and 3e).

Further, the XEL behavior was examined. Figure 3f demonstrates that the developed ultra-high-crystallinity transparent GC exhibits a strong XEL integrated intensity (approximately 94.2 % of that of the commercial BGO scintillator). As shown in Figure 3g, the absorption coefficients of GC are slightly weaker than those of BGO in the 1-10^3 keV range, suggesting that the intense XEL

intensity of the proposed GC is primarily due to its distinct structure. The X-ray absorption coefficients were calculated from the material compositions using the photon cross-section database of the National Institute of Standards and Technology. To be noted, studies on the temperature-dependent XEL intensity suggests the much-improved resistance to thermal quenching compared to commercial BGO and most previously reported scintillators (Figures 3h, S5, S6, Tables S4 and S5), particularly at high temperatures, with the developed GC maintaining 99.1 % intensity at 473 K (200 °C) and 90.6 % intensity at 573 K (300 °C), whereas the BGO only retains 4.8 % intensity at 473 K and 1.2 % intensity at 573 K. To achieve in-depth understanding, the X-ray excited thermoluminescence (TL) technique is utilized to monitor the detrapping behavior of immobilized charge carriers in defect centers as the temperature increases (Figure 3i). The TL spectrum exhibits intense thermal-induced emission during a broad temperature range from 300 K to 400 K, indicating that the achieved zero-thermal-quenching performance arises from the release of the carriers from the defects under the supplied thermal energy going beyond thermal barrier (the energy of trap depth). Then, the Hoogenstraaten method was employed to analyze the TL glow curve using the following equation[29]:

$$\frac{\beta E}{kT_m^2} = s\exp(-\frac{E}{kT_m}) \quad \text{(Equation 1)}$$

where E is the trap depth in eV, T_m the temperature (K) at the glow peak maximum, k the Boltzmann constant (eV/K) and s the frequency factor. By plotting $\ln(T_m^2/\beta)$ versus $1/kT_m$, (the inset of Figure 3i), trap depth is calculated as 0.69 eV from the slope of the linear fit. Meanwhile, electron paramagnetic resonance (EPR) results reveal an intense signal with g=2.003 for ultra-high-crystallinity GC after exposing to X-ray radiation for 5 min, which is characteristic EPR signal of oxygen vacancy defect ($V_O^{\bullet}$)[30]. In contrast, no obvious g = 2.003 signal is observed in

the non-irradiated GC (Figure S7), confirming X-ray-induced carrier trapping by oxygen-vacancy-related defects. Due to the highly localized nature and limited mobility of electrons trapped at defects within the amorphous phase, which restricts their ability to influence luminescent centers in the crystalline phase, these defects are most likely located within the crystal lattice or at the crystalline-amorphous interface.

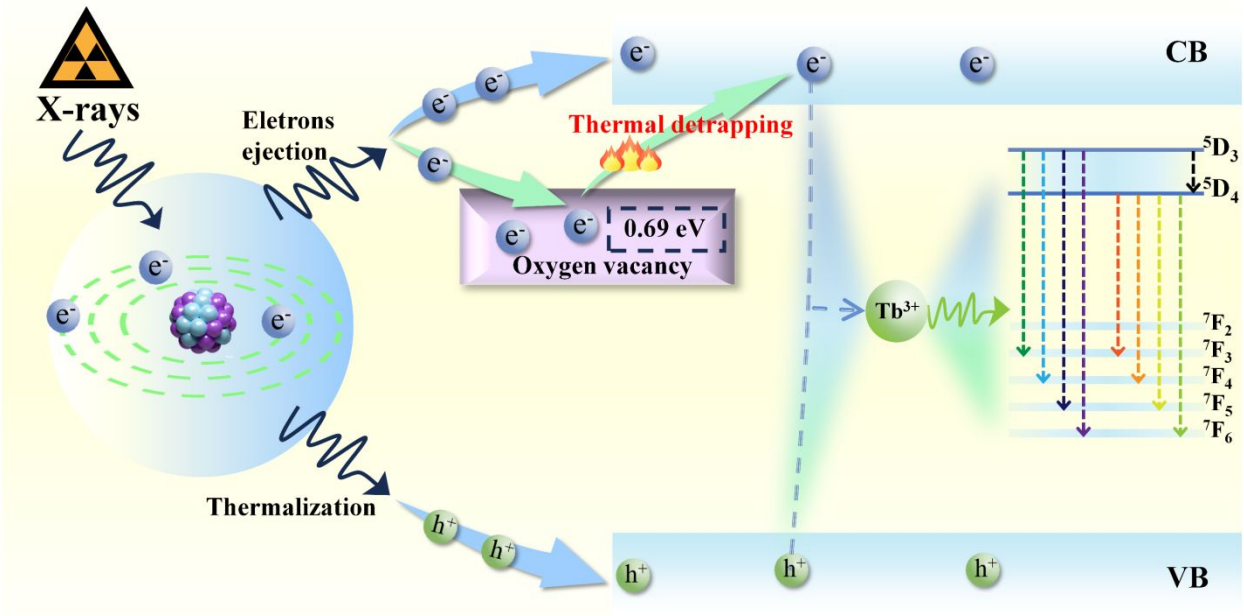

Figure 4. The possible X-ray-excited zero-thermal-quenching mechanism for the ultra-high-crystallinity GC, including the Tb^{3+} energy-level scheme and thermally stimulated carrier detrapping process.

As schematically illustrated in Figure 4, the possible X-ray excited zero-thermal-quenching mechanism for the ultra-high-crystallinity GC is proposed. (1) Upon irradiation by X-ray, incident X-ray photons interact with lattice atoms through the photoelectric effect and Compton scattering to generate hot electrons and deep holes, which then produce secondary electrons and holes via electron-electron scattering and the Auger process. The resulting charge carriers subsequently dissipate energy through thermal interactions with phonons, populating both the conduction band and the valence band with low-energy charge carriers. (2) The generated large number of electrons

and holes undergo non-radiative recombination and transfer the recombination energy to Tb^{3+} for luminescence, while portion of the electrons are simultaneously captured by $V_O^{\bullet\bullet}$ with trap depth of 0.69 eV and continuous energy distribution. (3) When the scintillator is exposed to high temperatures, a significant number of electrons trapped in $V_O^{\bullet\bullet}$ are thermally released, further promoting energy transfer to Tb^{3+}, enhancing the luminescent behavior.

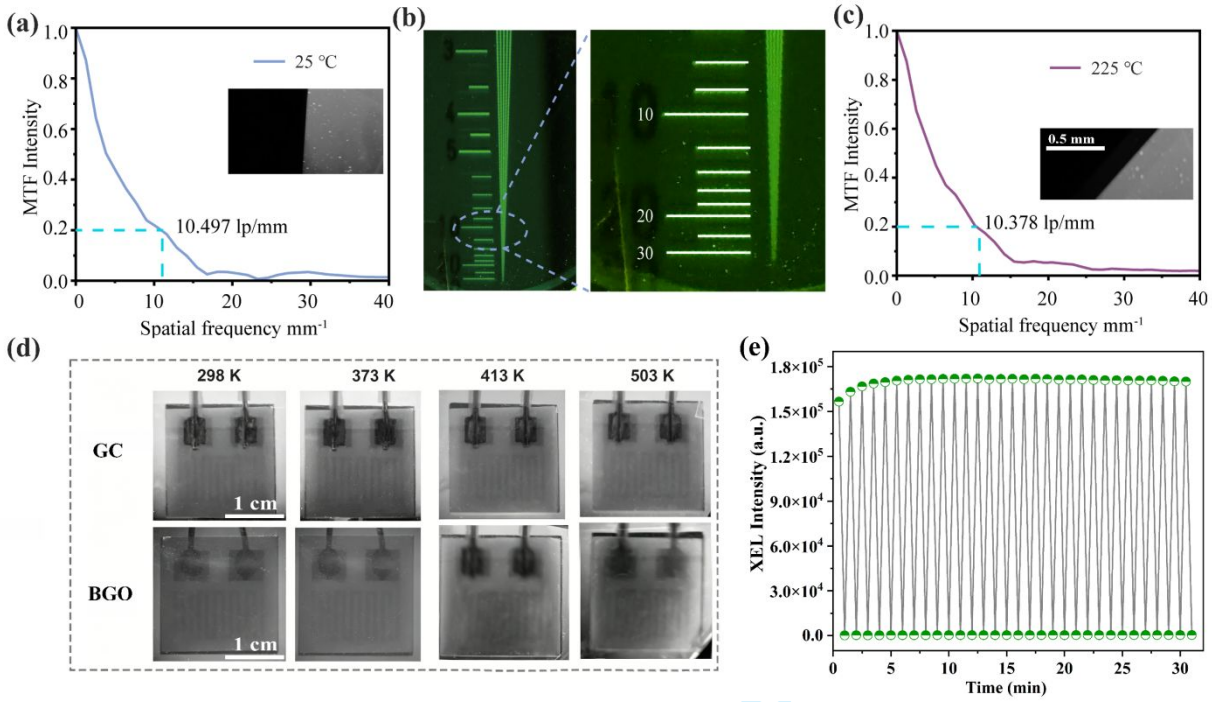

Figure 5. (a) MTF curve at 298 K (25 °C), with the spatial resolution of 10.497 lp/mm. (b) The X-ray images of the line pair card at 298 K (25 °C). (c) MTF curve at 498 K (225 °C) with the spatial resolution of 10.378 lp/m. (d) The comparison of the X-ray images from ultra-high-crystallinity GC and BGO at 298 K (25 °C)-503 K (230 °C). (e) Long-term XEL stability of GC.

The spatial resolution of the proposed ultra-high-crystallinity GC-based X-ray imaging system is quantified via modulation transfer function (MTF) analysis, edge spread function (ESF) imaging, and resolution imaging characterization. At ambient temperature (25 °C, Figure 5a), the system achieved a 20 % cutoff MTF of 10.497 lp/mm, with ESF images demonstrating sharp,

high-contrast edge transitions that confirm robust preservation of fine spatial details. Resolution phantom images (Figure 5b) further validate this resolving capability, as line-pair structures are clearly delineated up to spatial frequencies matching the MTF cutoff. Additional measurements show that the XEL intensity and MTF-derived imaging resolution both increase as the heat-treatment temperature rises from 700 to 850 °C, but decrease markedly at 900 °C (Figures S8, S9 and Table S6). This result suggests that the increase in crystallinity compensates for the slight transmittance loss below 850 °C, whereas excessive grain growth and Ostwald ripening at 900 °C reduce both transparency and crystallinity, thereby degrading the scintillation and imaging performance. These results indicate that crystallinity and optical transmittance jointly determine the overall scintillation performance and imaging behavior of glass-ceramic scintillators. To evaluate the temperature-dependent imaging performance, the MTF was further characterized over the temperature range of 75-225 °C (Figures 5c and S10), revealing that the spatial frequency corresponding to the 0.2 MTF criterion consistently remained at approximately 10.3 lp mm^{-1}, indicative of excellent thermal stability. Simultaneously, X-ray imaging of a star-shaped object was performed over a temperature range of 25-225 °C (Figure S11), revealing sharp and high-contrast radial spokes with well-defined edges at all tested temperatures, with only minor fluctuations in brightness uniformity observed at 225 °C. Moreover, as shown in Figure 5d, the GC scintillator retained sharp X-ray image contrast across 298 K (25 °C)-503 K (230 °C), with no observable blurring or loss of spatial detail. In contrast, the reference BGO scintillator exhibited noticeable image blurring and contrast degradation at temperatures above 413 K, consistent with known thermal quenching effects in bulk oxide scintillators. Further sharp-edge MTF analysis confirms this degradation, with the spatial resolution of BGO decreasing from 11.613 lp/mm at

298 K to 3.256 lp/mm at 503 K (Figure S12). These results highlight unique thermal stability of the present ultra-high-crystallinity GC which stems from its low phonon energy and robust crystal structure, addressing a critical limitation of conventional detectors in extreme-environment X-ray imaging scenario. Additionally, to assess long-term imaging applicability (X-ray tube operated at 40 kV and 30 mA), the XEL stability of the GC was evaluated over 30 min of continuous on-off cycling (Figures 5e and S13), during which the XEL intensity remained highly consistent, exhibiting only negligible fluctuations between successive cycles. Long-term XEL stability under continuous X-ray irradiation has been measured at RT, 50, 100, and 200 °C. As shown in Figure S14, the initial enhancement of XEL intensity in GC, caused by the "bright burn effect" in which defects compete with luminescent centers for charge carriers, eventually stabilizes as these defects become saturated, demonstrating the proposed material's excellent irradiation resilience under elevated temperature conditions.

3. Conclusion

In summary, an ultra-high-crystallinity transparent GC scintillator is developed via a controllable crystallization strategy using sequential precipitation, where cubic CaF_2 nanocrystals form first, promoting heterogeneous nucleation and growth of hexagonal $BaAl_2Si_2O_8$, with nanoscale phase separation reducing atomic diffusion distances and achieving 97.6 % crystallinity. More importantly, defect traps (oxygen vacancy defects) facilitate the efficient capture of carriers and their thermally stimulated release, thus conferring remarkable resistance to thermal quenching. Consequently, the proposed GC scintillator maintains 90.6 % of its integrated XEL intensity at 300 °C, with its integrated XEL intensity at room temperature reaching 94.2 % of the commercial BGO, enabling stable high-temperature X-ray imaging with a spatial resolution of ~10.4 lp/mm

up to 225 °C. This work overcomes the long-standing trade-offs between crystallinity, transparency, and thermal stability in GC scintillators, offering a universally applicable design framework for high-performance X-ray imaging scintillators operating under extreme thermal conditions.

4. Experimental sections:

Synthesis of dual-phase glass-ceramics. SiO_2 (Bodi, 99%), Al_2O_3 (Macklin, 99%), $BaCO_3$ (Macklin, 99%), CaF_2 (Macklin, 99%), and TbF_3 (Innochem Co., 99.9%) were employed as starting reagents. $BaAl_2Si_2O_8/CaF_2$ dual-phase GC were prepared via a conventional melt-quenching technique, followed by controlled heat-treatment-induced crystallization. For each batch, approximately 8 g of raw materials with the nominal composition of $60SiO_2$-$20Al_2O_3$-$20BaCO_3$-$20CaF_2$-$3TbF_3$ (mol%) was thoroughly mixed and ground for ~20 min to ensure compositional homogeneity. The powder mixture was then transferred into an alumina crucible and melted at 1600 °C in air to obtain a homogeneous melt, with the melting time fixed at 40 min. Subsequently, the melt was cast into a brass mold preheated to 350 °C and pressed to form bulk PG. To release residual internal stress, the as-cast PG were annealed at 400 °C for 12 h. The annealed PG were further heat-treated at 850 °C for 2.5 h to precipitate $BaAl_2Si_2O_8$ and CaF_2 crystalline phases, yielding $BaAl_2Si_2O_8/CaF_2$ dual-phase GC. Finally, all samples were cut and polished to the required dimensions for subsequent measurements. For the X-ray imaging experiments, the optimized GC scintillator was cut and polished into a 20 mm × 20 mm × 1 mm plate.

Characterization: Powder X-ray diffraction (XRD) patterns were collected to identify crystalline phases using an X-ray diffractometer (SmartLab, Rigaku) with Cu Kα radiation (λ = 0.154 nm)

operated at 40 kV and 50 mA. Data were recorded over the 2θ range of 10°-70° with a step size of 0.02° and a scanning rate of 10°·min^{-1}. The morphology and microstructure were examined by transmission electron microscopy (TEM; JEM-2010), and high-resolution TEM (HRTEM) was employed to resolve lattice fringes. Scanning transmission electron microscopy (STEM) in high-angle annular dark-field (HAADF) mode was performed on an aberration-corrected FEI Titan Cubed S-Twin microscope operated at 200 kV. Optical transmittance spectra of samples were measured on a spectrophotometer (Lambda 950) in the wavelength range of 400–800 nm. Solid-state ^{29}Si and ^{27}Al nuclear magnetic resonance (NMR) spectra were recorded on a Bruker Avance NEO 600 MHz spectrometer. Raman spectra were acquired using an Edinburgh Instruments RMS 1000 spectrometer equipped with a 785 nm laser, collected from 100 to 2000 cm^{-1} with an integration time of 100 s (exposure time: 10 s·cm^{-1}). Differential scanning calorimetry (DSC; Netzsch STA 449 F3) was carried out by heating ~20 mg of PG powder in an air atmosphere using an α-Al_2O_3 crucible at a heating rate of 10 °C·min^{-1} up to 1000 °C. Photoluminescence excitation (PLE) spectra, photoluminescence (PL) spectra, PL decay curves, and X-ray excited luminescence (XEL) spectra were measured on a fluorescence spectrometer (Edinburgh Instruments FLS1000) equipped with a 450 W continuous xenon lamp and a 12 W X-ray source. To calculate the modulation transfer function (MTF) using the slanted-edge method, X-ray images of a sharp aluminum edge (thickness: ~1.0 mm) were acquired. The edge spread function (ESF) was extracted from the edge profile, and the line spread function (LSF) was obtained by differentiating the ESF. The MTF was then calculated as the Fourier transform of the LSF, as described by the following formula:

$$MTF(\nu) = F(LSF(x)) = F\frac{dESF(x)}{dx}$$

Where the ν represents the spatial frequency, x is the position of pixels, and is defined by following formula:

$$x = \frac{N \cdot d}{\beta}$$

Where N is the ordinal number of pixels in the X-ray edge image, d is the pixel size, and β is the optical magnification.

Received XX; accepted XX; published online XX

1 Zhao S, Wu Y, Jin Z *et al.* Waterproof scintillator for efficient 3D X-ray imaging enabled by color and space reconfiguration. Matter, 2025, 8: 102261.

2 Ran P, Yang L, Hui J *et al.* Single-shot X-ray and near-infrared (NIR) dual-mode fusion imaging based on bifunctional NIR scintillators. Light Sci Appl, 2025, 14: 315.

3 Chen J, Li J, Yin T *et al.* Rb-Doped $Cs_3Cu_2I_5$ Perovskite nanocrystals as paper-based scintillator film for high-resolution X-ray imaging. Adv Funct Mater, 2025, 35: 2506331.

4 Ma J, Lu H, Yang J *et al.* Rational design and synthesis of a uranyl-organic hybrid for X-ray scintillation. Chin. J. Struct. Chem., 2024, 43: 100275.

5 Gao P, Kong Q, Sun Y *et al.* One-dimensional $(C_{12}H_{12}N)_3Cu_3I_6$ for high-performance direct X-ray detection. Chin. J. Struct. Chem., 2026, 45: 100767.

6 Li H, Li K, Li Z *et al.* Lanthanide-based metal halides prepared at room temperature by recrystallization method for X-ray imaging. Light Sci Appl, 2025, 14: 195.

7 Li L, Chen J, He G, Guo H. Tb^{3+}-doped phosphors-based-glass scintillators with excellent performance for high-temperature X-ray imaging. Laser Photonics Rev, 2026, 5: e02368.

8 Liu J, Zhao X, Xu Y *et al.* All-inorganic glass scintillators: scintillation mechanism, materials, and applications. Laser Photonics Rev, 2023, 17: 2300006.

9 He G, Li L, Chen J, Guo H. A thermal stable multi-functional Cu^{+}-doped glass for high-resolution X-ray imaging and full-spectra lighting. Laser Photonics Rev, 2025, 19: e00396.

10 He G, Chen J, Li L, Guo H. Cu^{+}-doped oxyfluoride glass with anti-thermal-quenching luminescence for X-ray imaging and WLED. J Adv Ceram, 2025, 14: 9221116.

11 Pan J, Lei J, Wei R *et al.* Eu^{2+}-doped transparent glass-ceramics with superior scintillation performance and stability for high-resolution X-ray imaging. Laser Photonics Rev, 2026, 6: e01906.

12 Fu J, Zhang Y, Ma Z *et al.* Crystallization kinetics of Al_2O_3-28mol%Lu_2O_3 glass and full crystallized transparent $Lu_3Al_5O_{12}$-based nanoceramics. Ceram Int, 2024, 50: 8073-8080.

13 Wang D, Zhang S, Chen J *et al.* Transparent glass composite scintillator with high crystallinity for efficient thermal neutron detection. Adv Funct Mater, 2024, 34: 2401992.

14 Zhu S, Jin S, Zhan L *et al.* Glass network engineering of yellow-emitting $Ba_2Sc_2B_4O_{11}$:Ce^{3+} glass ceramics for full-spectrum lighting. J Adv Ceram, 2025, 14: 9221169.

15 Zhang H, Huang X, Wan T *et al.* Integrated copper-halide activated scintillator fiber array for remote high-resolution X-ray imaging. Nat Commun, 2025, 16: 5973.

16 Wang D, Li H, Chen J *et al.* Congruent glass composite scintillator for efficient high-energy ray detection. Adv Mater, 2025, 37: 2412661.

17 You F, Lin S, Qiao X *et al.* Amorphous engineering of transparent high-crystallinity luminescent nano-glass-ceramics for advanced photonic applications. Adv Mater, 2026, 10: e20325.

18 Li L, Chen J, He G *et al.* Anti-thermal-quenching radio-luminescence and high-temperature X-ray imaging of Tb^{3+}-doped glass scintillators. Sci China Mater, 2026, 69: 761−771.

19 Liu Q, Ran P, Chen W, *et al.* Bright transparent scintillators with high fraction $BaCl_2:Eu^{2+}$ nanocrystals precipitation: an ionic-covalent hybrid network strategy toward superior X-ray imaging glass-ceramics. Adv Sci, 2023, 10: 2304889.

20 Wang S, Yang J, Liu C, *et al.* $KTb_{3-x}Gd_xF_{10}$ nano-glass composite scintillator with excellent thermal stability and record X-ray imaging resolution. Laser Photonics Rev, 2025, 19: 2401611.

21 Li K, Zhang W, Niu L *et al.* Lead-free cesium manganese halide nanocrystals embedded glasses for X-ray imaging. Adv Sci, 2023, 10: 2204843.

22 Pang T, Lin S, You F *et al.* Synergistic enhancement of crystallinity and transparency in Tb^{3+}-doped nano-glass-ceramics for high-resolution X-ray imaging. J Adv Ceram, 2025, 14: 9221122.

23 Wu M, Yu M, Cheng X *et al.* Energy transfer study on dense and transparent Eu^{3+}/Tb^{3+}-coactivated TeO_2-Gd_2O_3-WO_3-ZnO glass scintillators. J Rare Earths, 2025, 43: 1364-1372.

24 Guo J, Chen J, Li L *et al.* Ce^{3+}-doped $Sr_{0.84}(Lu,Gd)_{0.16}F_{2.16}$ glass-ceramics scintillators for high resolution X-ray imaging. J Rare Earths, 2025: S1002072125002376.

25 Zhang W, Liu J, Cui Y *et al.* Transparent oxyhalide glass-ceramic scintillators containing lead-free chloride perovskite nanocrystals for high-resolution and stable X-ray imaging. Sci China Mater, 2026.

26 Bai M, Zhang R, Guo J *et al.* Multilevel encapsulation-engineered ultra-stable flexible scintillator films for high-resolution X-ray imaging. Sci China Mater, 2026, 69: 1440–1447.

27 Ma W, Jiang T, Yang Z *et al.* Highly resolved and robust dynamic X-ray imaging using perovskite glass-ceramic scintillator with reduced light scattering. Adv Sci, 2021, 8: 2003728.

28 Liu Q, Ran P, Chen W *et al.* Bright transparent scintillators with high fraction $BaCl_2 : Eu^{2+}$ nanocrystals precipitation: An ionic-covalent hybrid network strategy toward superior X-ray imaging glass-ceramics. Adv Sci, 2023, 10: 2304889.

29 Lin C, Wu Z, Ma H *et al.* Charge trapping for controllable persistent luminescence in organics. Nat Photon, 2024, 18: 350-356.

30 Bai X, Liao J, Lou B *et al.* Reversible photochromism and multicolor luminescence modulation for X-ray detection and secure information encryption. Adv Funct Mater, 2026, 36: e06583.

Acknowledgements

This research was supported by National Natural Science Foundation of China (12304442, 52572155, 52272141), Natural Science Foundation of Fujian Province (2024J02014, 2024J01949), Natural Science Foundation of Fujian for Excellent Young Scholars (2026J009042), and National Innovative Training Program for College Student of China (cxxl-2026089).

Author contributions

S. S. Lin conceived the material design and wrote the first draft. R. J. Gu and Y. F. Zhang synthesized the material. S. S. Lin, J. D. Lin and D. Q. Chen helped to analyze the experimental results, and S. S. Lin finalized the manuscript. X. S. Qiao helped to perform the molecular dynamics simulations. J. D. Lin, L. W. Zeng and H. W. Lin assisted with the measurements. J. D. Lin and X. X. Yang assisted with the X-ray imaging measurements. J. D. Lin, X. H. Xu, F. Huang, and D. Q. Chen provided constructive suggestions for data analysis. D. Q. Chen supervised the project.

Conflict of interest

Experimental details and supporting data are available in the online version of the paper.

Supplementary information

Experimental details and supporting data are available in the online version of the paper.

Shisheng Lin received his PhD degree from Fujian Institute of Research on the Structure of Matter, Chinese Academy of Sciences, in 2021. He is presently an associate professor at Fujian Normal University. His research mainly focuses on photofunctional glass-ceramics and ceramics.

Yunfei Zhang is presently a master's degree candidate. He received his bachelor's degree from Shanxi University in 2019. His research mainly focuses on glass-ceramics.

Jidong Lin received Ph.D. in condensed matter physics from Fujian Normal University in 2024. He is currently an experimentalist at the School of Physics and Energy, Fujian Normal University, and his current research interests focus on optoelectronic materials and display applications.

Daqin Chen received his PhD degree from Fujian Institute of Research on the Structure of Matter, Chinese Academy of Sciences, in 2008. He is presently a professor at Fujian Normal University. His research mainly focuses on luminescent materials and devices.

Xiuxia Yang received her PhD degree from Fujian Institute of Research on the Structure of Matter, Chinese Academy of Sciences, in 2024. She is presently a lecturer at Kunming University of Science and Technology. Her research mainly focuses on mechanoluminescent materials, persistent luminescent materials, and rare-earth-doped glass-ceramics.

用于高温 X 射线成像的超高结晶度透明玻璃陶瓷闪烁体

林世盛[+]，张云飞[+]，顾儒健，林继栋[*]，乔旭升，曾令玮，林何雯，郑嘉敏，杨秀霞[*]，徐旭辉，黄烽，陈大钦[*]

摘要 高温 X 射线成像对闪烁体的结晶度、闪烁效率、热稳定性等方面提出了严苛要求。然而，当前适用的闪烁材料仍十分匮乏。鉴于此，本研究通过可控热处理诱导析晶的方式，设计并制备了一种超高结晶度的透明玻璃陶瓷（GC）闪烁体。该材料具有分步析晶机制，即立方 CaF_2 纳米晶首先形成，随后促使六方 $BaAl_2Si_2O_8$ 在其表面实现异质形核与生长。同时，材料内部存在的 F 富集区与 O 富集区形成了本征纳米尺度相分离，有效缩短了原子扩散距离，从而实现了高达 97.6 %的超高结晶度。值得注意的是，氧空位等缺陷能级可能位于晶格内部或晶相/非晶相界面，能够高效俘获载流子并在热激发下释放，从而赋予材料显著的抗热猝灭能力。因此，所制备的 GC 闪烁体在 300 °C 下仍可保持室温 X 射线激发发光（XEL）积分强度的 90.6 %，其室温积分 XEL 强度达到商业 $Bi_4Ge_3O_{12}$（BGO）的 94.2%。在此基础上，实现了在高达 225 °C 的环境下稳定的高温 X 射线成像，其空间分辨率约为 10.4 lp/mm。本研究为开发适用于极端环境的高灵敏度 X 射线闪烁体提供了一种有效途径。

Supporting Information

Ultra-High-Crystallinity Transparent Glass-Ceramic Scintillators for High-Temperature X-Ray Imaging

Shisheng Lin [1, +], Yunfei Zhang [1, +], Rujian Gu [1], Jidong Lin [1, *], Xusheng Qiao [2], Lingwei Zeng [3], Hewen Lin [1], Jiamin Zheng [1], Xiuxia Yang [4, *], Xuhui Xu [4], Feng Huang [1], Daqin Chen [1, 5, *]

[1] Dr. S. S. Lin, Y. F. Zhang, R. J. Gu, J. D. Lin, H. W. Lin, J. M. Zheng, Prof. F. Huang, Prof. D. Q. Chen
College of Physics and Energy, Fujian Normal University, Fuzhou, 350117, P. R. China
E-mail: jdlin@fjnu.edu.cn (J. D. Lin); dqchen@fjnu.edu.cn (D. Q. Chen)

[2] Dr. X. S. Qiao
State Key Laboratory of Silicon Materials & School of Materials Science and Engineering, Zhejiang University, Hangzhou, 310027, P. R. China

[3] Dr. L. W. Zeng
School of Chemistry and Chemical Engineering, Hunan University of Science and Technology, Xiangtan, 411201, P. R. China

[4] Dr. X. X. Yang, Prof. X. H. Xu
Faculty of Materials Science and Engineering, Key Laboratory of Advanced Materials of Yunnan Province, Kunming University of Science and Technology, Kunming, 650093, P. R. China
E-mail: xiuxia941129@163.com (X. X. Yang);

[5] Prof. D. Q. Chen
Fujian Provincial Engineering Technology Research Center of Solar Energy Conversion and Energy Storage, Fuzhou, 350117, P. R. China

[+] These authors contributed equally to this work

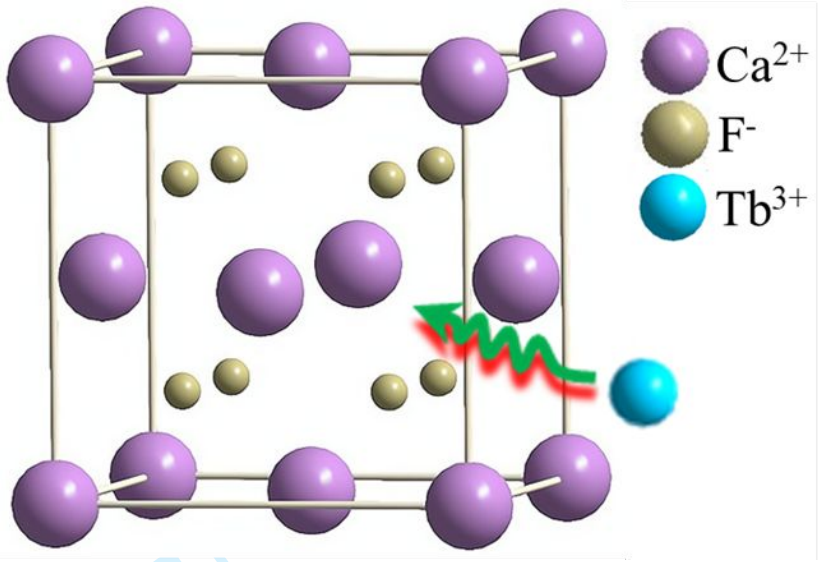

Figure S1. Schematic illustration of the CaF_2 crystal structure showing substitutional doping of Tb^{3+} ions at Ca^{2+} sites.

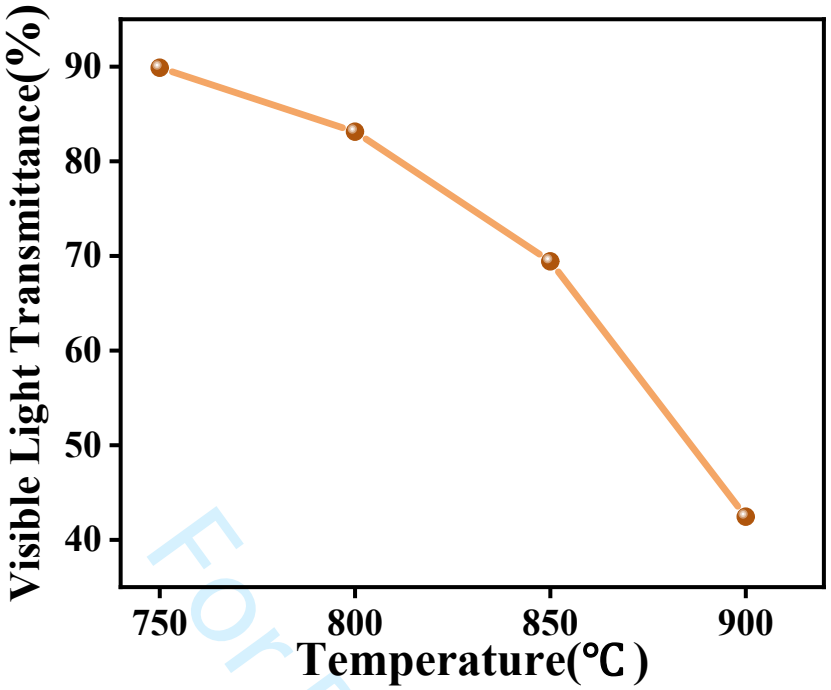

Figure S2. Visible light transmittance of the GC prepared at different heat-treatment temperatures.

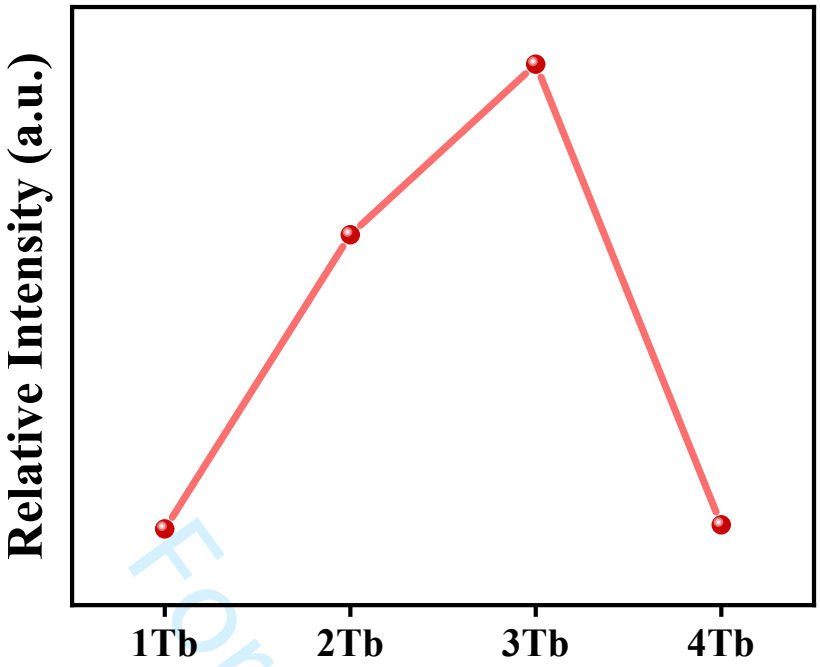

Figure S3. Relative intensity extracted from the XEL spectra for Tb^{3+}-doped samples with different Tb contents (1Tb, 2Tb, 3Tb, and 4Tb).

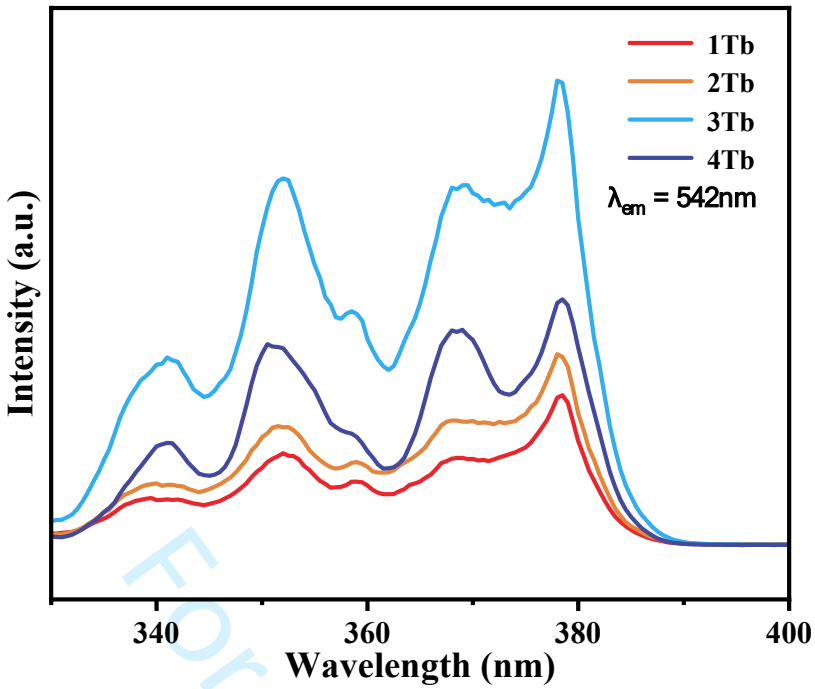

Figure S4. Photoluminescence excitation (PLE) spectra of Tb^{3+}-doped samples with different Tb contents (1Tb, 2Tb, 3Tb, and 4Tb) via monitoring emission at 542 nm.

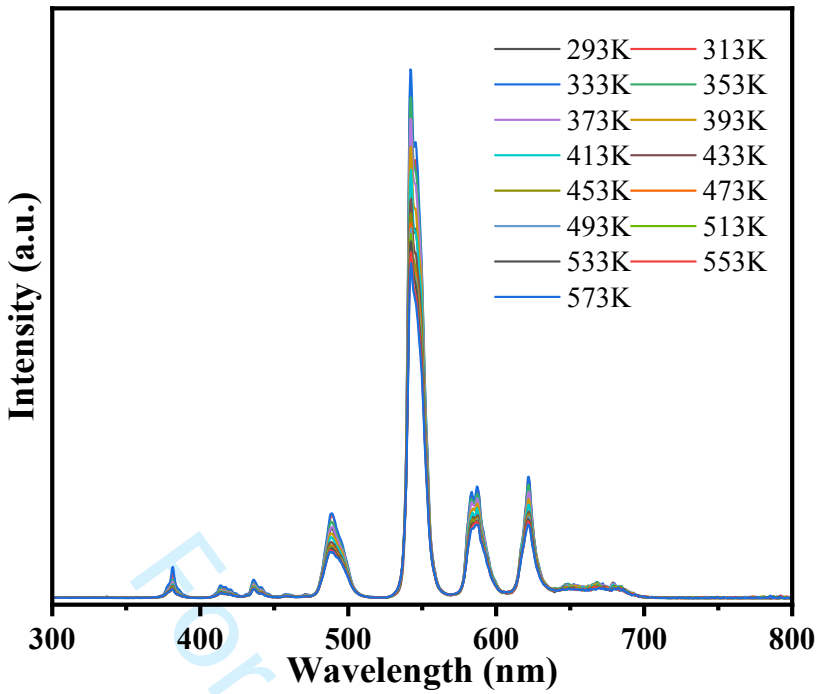

Figure S5. Temperature-dependent XEL spectra of the GC recorded at 293~573 K.

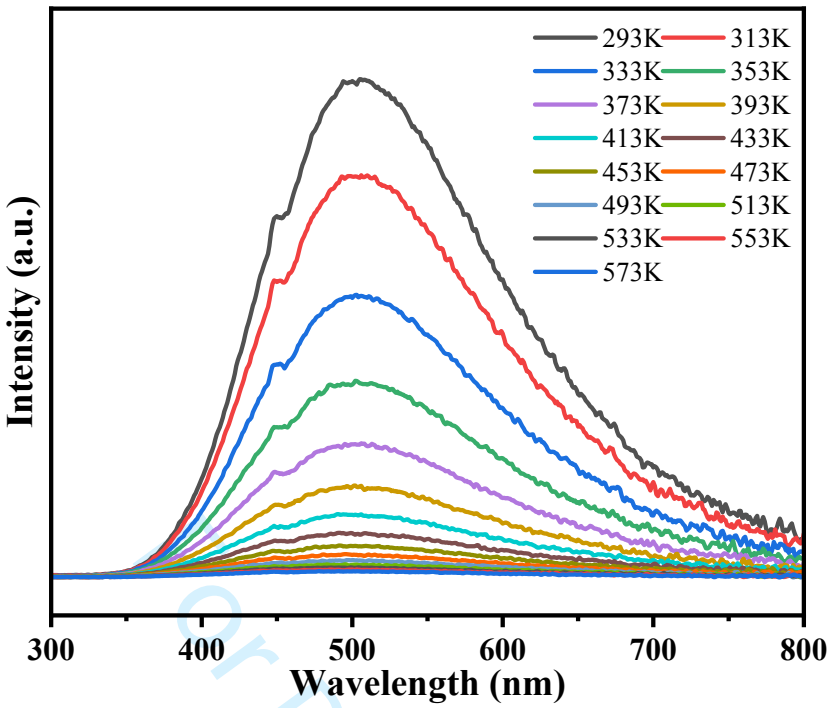

Figure S6. Temperature-dependent XEL spectra of the BGO recorded at 293~573 K

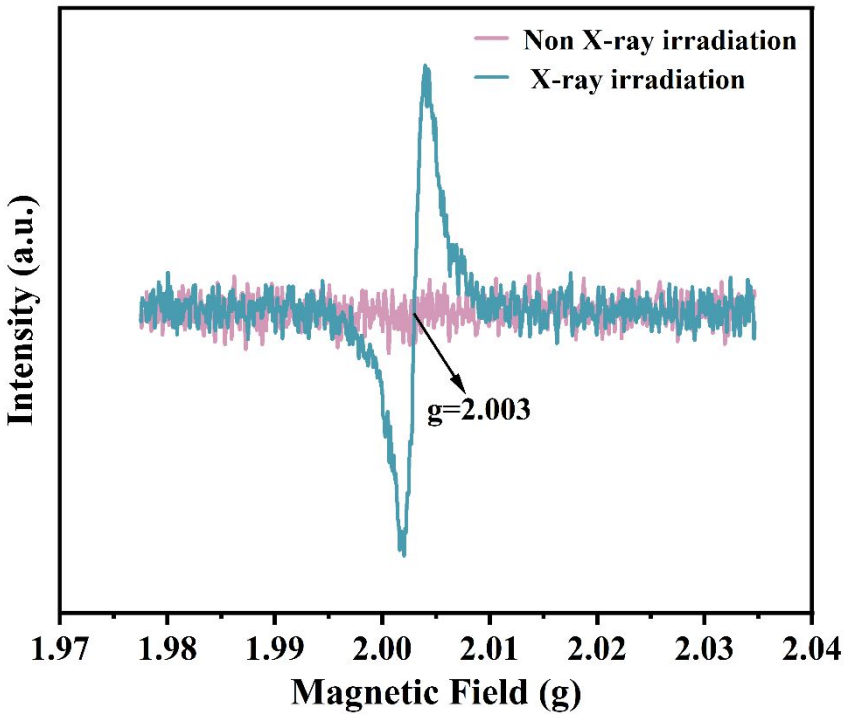

Figure S7. EPR spectra of the pristine non-irradiated GC and the GC after 5 min of X-ray irradiation.

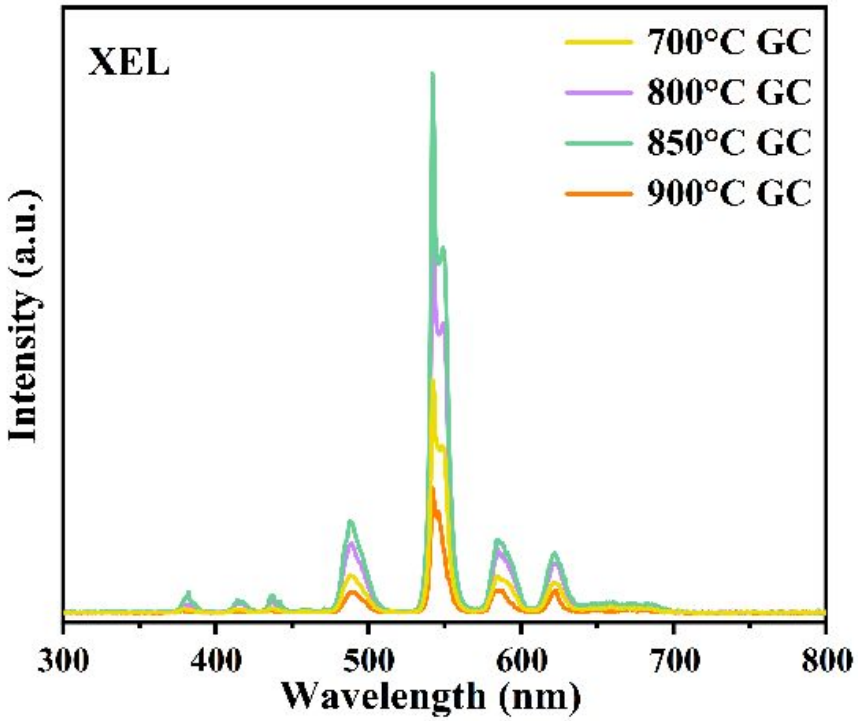

Figure S8 XEL spectra of the GC heat-treated at different temperatures of 700, 800, 850, and 900 °C under X-ray excitation.

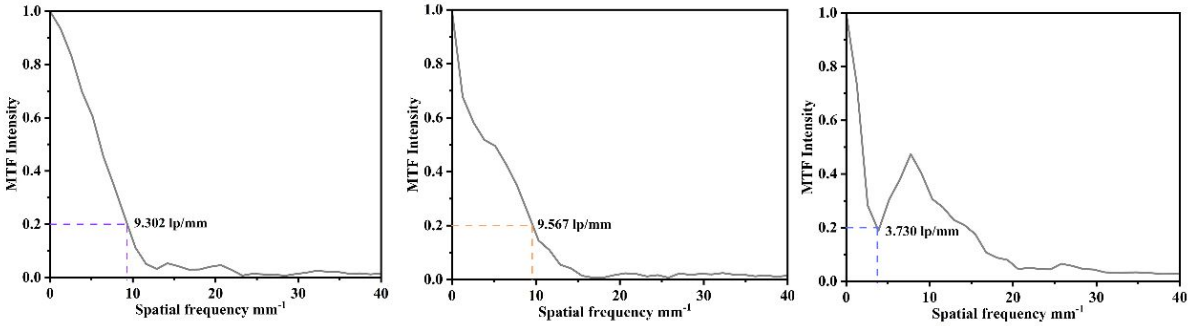

Figure S9 MTF curves of the GC subjected to different heat-treatment temperatures.

(a) 700 °C GC, (b) 800 °C GC, and (c) 900 °C GC.

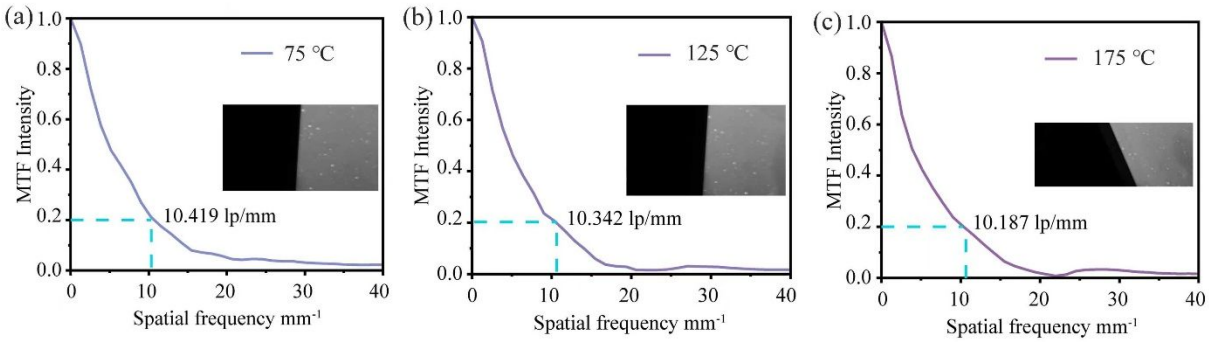

Figure S10. MTF curves of the proposed ultra-high-crystallinity GC measured over the temperature range of 75-175 °C.

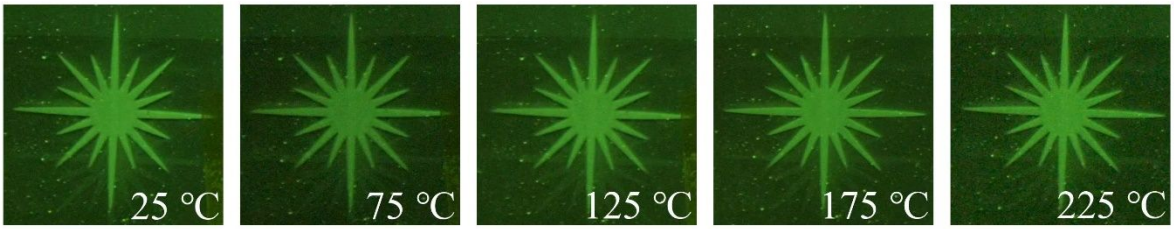

Figure S11. Temperature-dependent X-ray imaging of a star-shaped object from 25 to 225 °C for the proposed ultra-high-crystallinity GC.

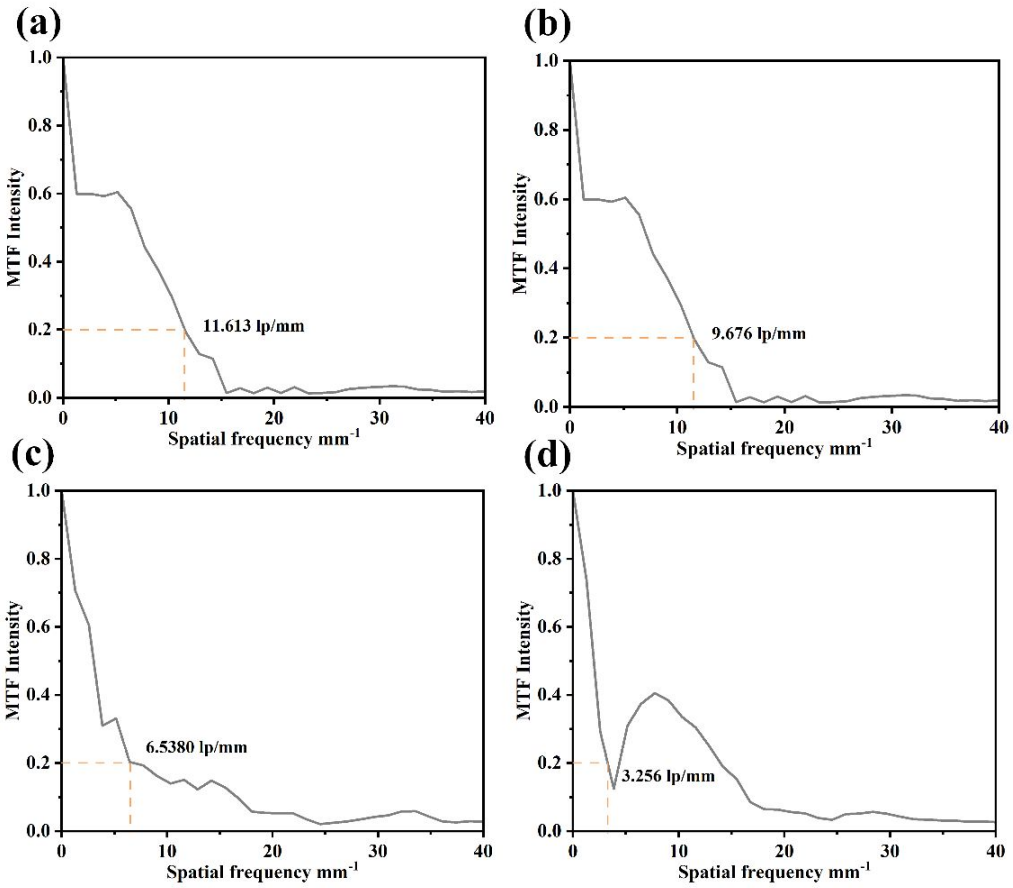

Figure S12. MTF curves of commercial BGO measured over the temperature range of 298–503 K. (a) 298 K, (b) 373 K, (c) 413 K, and (d) 503 K.

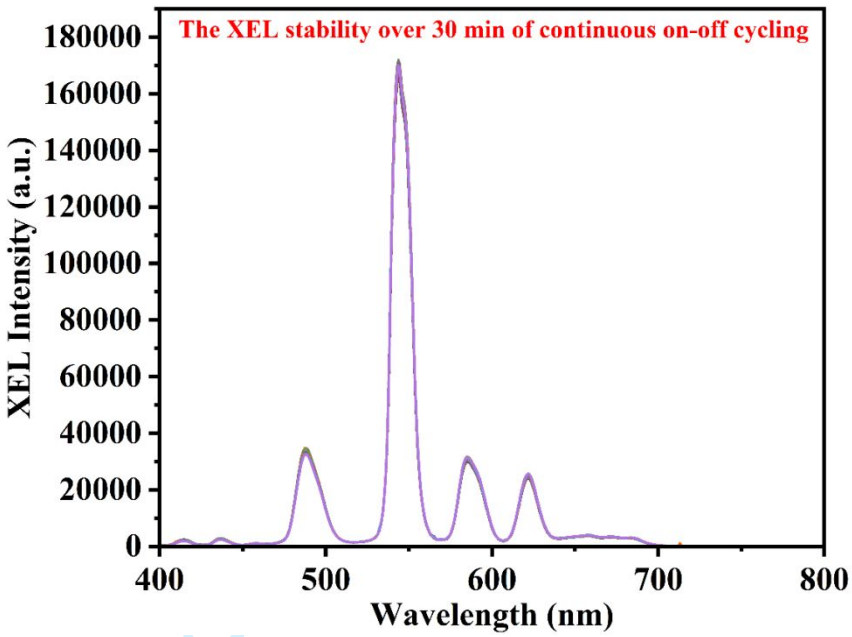

Figure S13. XEL spectra of the GC scintillator measured during 30 min continuous on-off irradiation cycling.

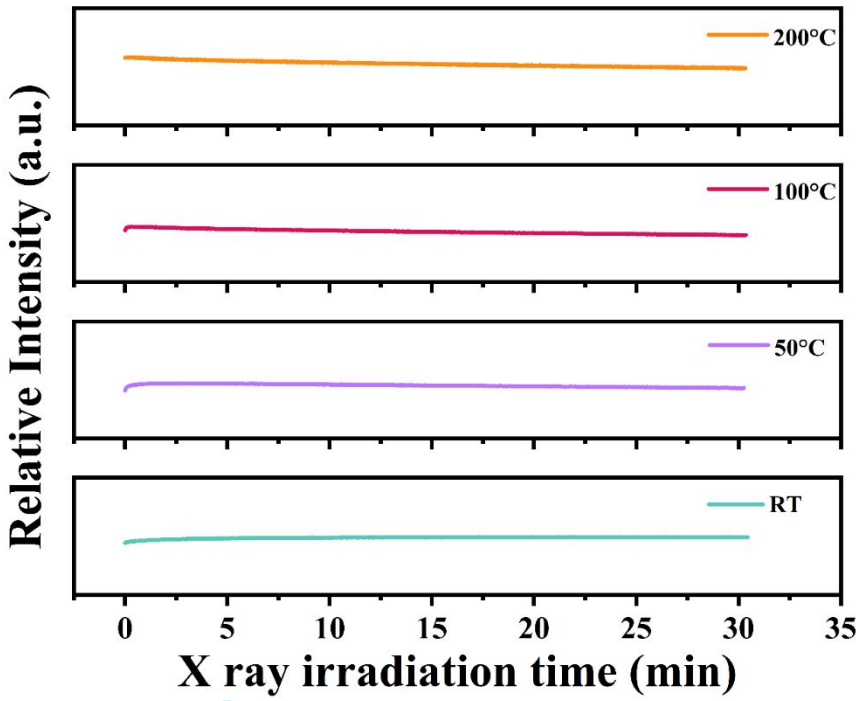

Figure S14. Long-term XEL stability of the GC during continuous X-ray irradiation at RT, 50, 100, and 200 °C.

Table S1 Comparison of crystallinity and transmittance of the present $BaAl_2Si_2O_8/CaF_2:Tb^{3+}$ glass-ceramic with those of representative transparent glass/glass-ceramic scintillators and related transparent glass-ceramic systems.

System	Crystallinity (%)	Transmittance (% @wavelength)	Reference
$BaAl_2Si_2O_8/CaF_2:Tb^3$	97.6	69.4% @ visible light	This work
$Bi_{0.8}Nb_{0.8}Te_{2.4}O_8$	~97	~67% @ 2.5 μm	1
$Mg_2Al_4Si_5O_{18}$	97	74% @ 400 nm	2
KYF_4	~72	~88% @ 900 nm	3
$Li(Al_7B_4O_{17})$	67.9	79.5% @ 550 nm	4
$NaLuF_4$	58	90% @ 542 nm	5
$ZnAl_2O_4$+$MgAl_2O_4$	47.17	78% @ visible light	6
$NaYP_2O_7$	27.16	57.84% @700 nm	7
$CsPbBr_3$	-	70% @500-800 nm	8
$CsEuBr_3$	20.7	70% @500 nm	9

Table S2. Crystallinity of the GC with different heat-treatment temperatures.

Temperature (℃)	Crystallinity (%)
700	7.97 %
750	23.52 %
800	24.43 %
850	97.63 %
900	83.05 %

Discussions on Table S2:

Further increasing the heat treatment temperature to 900 °C reduced the crystallinity to 83.05 %, likely due to Ostwald ripening, thereby identifying 850 °C as the optimal heat treatment temperature.

Table S3. Peak-fitting results of deconvoluted ^{29}Si and ^{27}Al MAS NMR spectra for PG and GC samples (Area, FWHM, and center) assigned to Q^n (Q^1-Q^4) and Al coordination species ([AlO_4] and [AlO_6]).

		Area	FWHM (ppm)	Center
Si PG	Q^1	9.81339×10^5	10.1958	-80.6163
	Q^2	2.218814×10^6	11.51336	-84.6163
	Q^4	5.50280×10^5	11.14281	-106.36682
Si GC	Q^1	6.67547×10^5	5.5153	-81.5411
	Q^2	2.490716×10^6	4.33667	-87.27888
	Q^3	2.63141×10^5	3.22287	-92.01363
	Q^4	1.770005×10^6	15.60399	-107.0626
Al PG	[AlO_{4a}]	4.04193×10^7	14.42658	59.37418
	[AlO_{4b}]	2.28401×10^7	23.97821	52.70934
	[AlO_6]	8.70439×10^5	5.68648	-0.5747
Al GC	[AlO_{4a}]	4.13274×10^7	12.819	59.92334
	[AlO_{4b}]	2.96939×10^7	21.87787	54.70721

Table S4 Integrated XEL intensities of commercial BGO and GC at different temperatures.

Temperature (K)	Integrated XEL intensity of BGO (a.u.)	Integrated XEL intensity of GC (a.u.)	GC /BGO(%)
298	1.36568×10^{7}	1.28647×10^{7}	94.2
473	6.55526×10^{5}	1.27489×10^{7}	1944.8
573	1.63882×10^{5}	1.16554×10^{7}	7112.1

Table S5 Comparison of thermal-quenching resistance under X-ray excitation for representative scintillators.

System	integrated XEL intensity (%)	Temperature (K)	Reference
$BaAl_2Si_2O_8/CaF_2:Tb^{3+}$ GC	90.6	573	**This work**
Ce^{3+}/Tb^{3+} doped glass	168	573	10
Tb^{3+} doped glass	143	633	11
Tb^{3+} PBG	100	573	12
$Sr_{0.84}Tb_{0.16}F_{2.16}$ GC	100	573	13
Cu^{+} doped oxyfluoride glass	63	573	14
Mn^{2+} doped glass	61	573	15
Mn^{2+} doped oxyfluoride glass	64	453	16
Eu^{2+}doped oxyfluoride glass	66.2	423	17
CaF_2: Eu^{2+} GC	80	473	18

Table S6. Crystallinity, transmittance, relative integrated XEL intensity, and room-temperature spatial resolution of the GC heat-treated at different temperatures.

Heat-treatment temperature (°C)	Crystallinity (%)	Transmittance (%)	Integrated XEL intensity (% BGO)	Spatial resolution (lp/mm)
700	7.97	89.8	41.9	9.302
800	24.43	83.1	74.5	9.567
850	97.63	69.4	94.2	10.497
900	83.05	42.4	21.3	3.730

Supplementary Note 1. XRD-based crystallinity calculation via peak deconvolution and amorphous halo subtraction.

Based on the diffraction features of crystalline and amorphous phases in glass-ceramic materials, the crystallinity can be quantified by separating and evaluating their contributions in the XRD pattern. Using the peak area method, the XRD pattern is deconvoluted to distinguish crystalline peaks from the amorphous hump. The total area of the crystalline peaks (A_c) and the area of the amorphous hump (A_a) are calculated, and the crystallinity (X_c) is determined by the following formula:

$$X_c = \frac{A_c}{A_c + A_a} \times 100\% \quad (1)$$

Supplementary Note 2. Computational details of molecular dynamics simulations.

The atomic-scale structural evolution of the precursor glass was investigated using molecular dynamics simulations via the DL_POLY 2.20 package. The glass model was constructed according to the nominal composition of the experimentally prepared precursor glass. The effective partial charge pairwise potentials, developed by Teter and modified by Du and Cormack, were employed to describe the interatomic interactions. A system containing approximately 3000 atoms was first equilibrated at 5000 K for 0.5 ns under the NVT ensemble, then quenched to 300 K at a cooling rate of 5 K/ps under the NPT ensemble, followed by final relaxation under the NVE ensemble. The Buckingham potential with Ewald summation and a cutoff distance of 12 A was used to describe the short-range and long-range interactions. The final relaxed atomic configuration was used to analyze the nanoscale spatial distribution of F- and O-containing structural units, thereby providing structural evidence for the F-enriched and O-enriched domains shown in Figure 2b.

Supplementary Note 3. Site-occupancy calculation of Tb^{3+} in $BaAl_2Si_2O_8$:

The site-selective occupancy of Tb^{3+} in hexagonal $BaAl_2Si_2O_8$ was evaluated using the Universal Point Edge Transformer (UPET) framework with the PET-OMat pre-trained machine-learning potential. A supercell of hexagonal $BaAl_2Si_2O_8$ was constructed, and one host cation was substituted by one Tb ion at different crystallographic sites, including Si, Ba, and Al sites. All substitutional configurations were fully relaxed using the BFGS optimizer with a force convergence criterion of 0.01 eV/A. The formation energy of each substitutional configuration was calculated relative to the pristine $BaAl_2Si_2O_8$ host and corresponding elemental reference states. The lower formation energy indicates a more energetically favorable occupation site. The calculated formation energies were then compared to determine the preferred Tb^{3+} occupation site in $BaAl_2Si_2O_8$, as shown in Figure 2c.

Supplementary references

1 Wen S, Wang Y, Lan B *et al.* Pressureless crystallization of glass for transparent nanoceramics. Adv Sci, 2019, 6: 1901096.

2 Tang W, Zhang Q, Luo Z *et al.* CoO-doped MgO-Al_2O_3-SiO_2-colored transparent glass-ceramics with high crystallinity. Appl Phys A, 2018, 124: 191.

3 Sun Y, Xiong P, Wu M *et al.* Crystal engineering of oxyfluoride glass with increased crystallinity and transmittance towards enhanced luminescence. Ceram Int, 2023, 49: 34845-34852.

4 Hu S. Modulation of structure and properties in Li_2O-Al_2O_3-B_2O_3 glass-ceramics through TiO_2 and P_2O_5 additives. Ceramics-Silikáty, 2024: 54–62.

5 Pang T, Lin S, You F *et al.* Synergistic enhancement of crystallinity and transparency in Tb^{3+}-doped nano-glass-ceramics for high-resolution X-ray imaging. J Adv Ceram, 2025, 14: 9221122.

6 Ren B, Hao H, Liu Y *et al.* High-alumina and low-lithium glass-ceramics modulated by heat treatment and its structural evolution mechanism. J Eur Ceram Soc, 2024, 44: 116723.

7 Liang H, Lin X, Ma N *et al.* High color-purity broad orange-red emission of Mn^{2+}-doped transparent phosphate glass-ceramics embedded $NaYP_2O_7$ crystals. J Am Ceram Soc, 2024, 107: 4977−4990.

8 Wei X, Zhang R, Li X, Xu Z, Gou Y. A highly stable $CsPbBr_3$-SiO_2 transparent glass ceramic by pressureless sintering for white LEDs. J Alloy Compd, 2025, 1031: 180725.

9 Li K, Long Z, Ye Y *et al.* Lead-free cesium europium bromide perovskite nanocrystals in glass for white light-emitting diode and X-ray imaging. Chem Eng J, 2025, 507: 160795.

10 Li L, Chen J, He G, Qiao X, Guo H. Achieving anti-thermal-quenching in Tb^{3+}-doped glass scintillators via dual-channel thermally enhanced energy transfer. J Adv Ceram, 2024, 15: 9221220.

11 Li L, Chen J, He G *et al.* Anti-thermal-quenching radio-luminescence and high-temperature X-ray imaging of Tb^{3+}-doped glass scintillators. Sci China Mater, 2026, 69: 761–771.

12 Li L, Chen J, He G, Guo H. Tb^{3+}-doped phosphors-based-glass scintillators with excellent performance for high-temperature X-ray imaging. Laser Photonics Rev, 2026, 20: e02368.

13 Li L, Chen J, He G, Qiao X, Guo H. High transparent $Sr_{0.84}Tb_{0.16}F_{2.16}$ glass-ceramic scintillators with excellent thermal stability for high-temperature X-ray imaging. Adv Opt Mater, 2025, 13: e01331.

14 He G, Chen J, Li L, Guo H. Cu^{+}-doped oxyfluoride glass with anti-thermal-quenching luminescence for X-ray imaging and WLED. J Adv Ceram, 2025, 14: 9221116.

15 Li L, Su Q, Chen J *et al.* Mn^{2+}-doped glass scintillators with anti-thermal quenching for high-temperature X-ray imaging. Chin Opt Lett, 2025, 23: 111602.

16 He G, Li L, Chen J, Chen L, Guo H. Rare-earth-free Mn^{2+}-activated glass for high-resolution X-ray imaging. Ceram Int, 2025, 51: 42338–42343.

17 Zou J, Li L, Chen J *et al.* Eu^{2+}-doped oxyfluoride glass scintillator for X-ray imaging. J Alloy Compd, 2025, 1020: 179428.

18 Wang W, Wang T, Tang H *et al.* High temperature and water stable CaF_2:Eu^{2+} glass ceramic for high resolution X-ray detection. J Alloy Compd, 2023, 956: 170361.